



RESEARCH ARTICLE

10.1029/2019JA027648

Special Section:

Probing the Magnetosphere through Magnetoseismology and Ultra-Low-Frequency Waves

The Changing Eigenfrequency Continuum During Geomagnetic Storms: Implications for Plasma Mass Dynamics and ULF Wave Coupling

S. J. Wharton¹ , I. J. Rae² , J. K. Sandhu² , M.-T. Walach³ , D. M. Wright¹ , and T. K. Yeoman¹ ¹Department of Physics and Astronomy, University of Leicester, Leicester, UK, ²Mullard Space Science Laboratory, University College London, Dorking, UK, ³Physics Department, Lancaster University, Lancaster, UK

Key Points:

- We measure the average storm time evolution of field line eigenfrequencies, accounting for diurnal variation
- Lower eigenfrequencies during the main phase for $L > 4$ are due to a weaker magnetic field and enhanced plasma mass density
- Higher eigenfrequencies during the main phase for $L < 4$ are due to plasmaspheric erosion

Supporting Information:

- Supporting Information S1

Correspondence to:

S. J. Wharton,
sjw136@le.ac.uk

Citation:

Wharton, S. J., Rae, I. J., Sandhu, J. K., Walach, M.-T., Wright, D. M., & Yeoman, T. K. (2020). The changing eigenfrequency continuum during geomagnetic storms: Implications for plasma mass dynamics and ULF wave coupling. *Journal of Geophysical Research: Space Physics*, 125, e2019JA027648. <https://doi.org/10.1029/2019JA027648>

Received 15 NOV 2019

Accepted 12 MAY 2020

Accepted article online 15 MAY 2020

Abstract Geomagnetic storms are one of the most energetic space weather phenomena. Previous studies have shown that the eigenfrequencies of ultralow frequency (ULF) waves on closed magnetic field lines in the inner magnetosphere decrease during storm times. This change suggests either a reduction in the magnetic field strength and/or an increase in its plasma mass density distribution. We investigate the changes in local eigenfrequencies by applying a superposed multiple-epoch analysis to cross-phase spectra from 132 geomagnetic storms. Six ground magnetometer pairs are used to investigate variations from approximately $3 < L < 7$ and across the whole dayside sector. We find that at $L > 4$, the eigenfrequencies decrease by as much as 50% relative to their quiet time values. Both a decrease in magnetic field strength and an increase in plasma mass density, in some locations by more than a factor of 2, are responsible for this reduction. The enhancement of the ring current and an increase in oxygen ion density could explain these observations. At $L < 4$, the eigenfrequencies increase due to the decrease in plasma mass density caused by plasmaspheric erosion.

Plain Language Summary Periods of intense solar wind can cause geomagnetic storms, large disturbances of the magnetosphere. Previous studies have shown that this can decrease the resonant frequencies of magnetic field lines with the Earth's magnetosphere. We perform a large statistical study on 132 storms to investigate this in order to understand the physics that drives this change. We find that the resonant frequencies typically decrease on field lines where $L > 4$ due to a weaker magnetic field caused by an enhanced ring current and a higher plasma mass density. We suggest the higher plasma mass density could be caused by an increase in Oxygen ions. At $L < 4$, the eigenfrequencies increase due to a drop in plasma mass density caused by plasmaspheric erosion.

1. Introduction

Geomagnetic storms are prolonged periods of intense solar wind-magnetosphere coupling that compress the Earth's magnetosphere, energize the magnetosphere-ionosphere system, and result in strong enhancements of the ring current, among other phenomena. These have been documented since the nineteenth century (Stewart, 1861). Coronal mass ejections and corotating interaction regions are the most common drivers of geomagnetic storms. The most intense coupling happens if the interplanetary magnetic field (IMF) is orientated southward and results in enhanced plasma convection within the magnetosphere (Akasofu et al., 1963; Gonzalez et al., 1994). During these disturbances, large quantities of energy are released from the Earth's magnetotail, often causing increased substorm activity (e.g., Hutchinson et al., 2011) and enhancing the Earth's radiation belts (e.g., Murphy et al., 2016).

The presence of a geomagnetic storm is usually monitored using ring current indices, most commonly the Dst <https://wdc.kugi.kyoto-u.ac.jp/dst/dir/dst2/onDstindex.html> or the Sym-H (Iyemori, 1990) index. Ring current indices are determined from the perturbation of the horizontal magnetic field strength using a set of ground-based magnetometers located at midlatitudes. These locations map to inside the ring current region of space where they largely avoid other current systems. A storm usually has three observable phases in the ring current indices (see Figure 1). During the initial phase, the ring current index increases due to the enhancements in the magnetopause currents as the magnetosphere is compressed, which increases the magnetic field strength on the ground. During the main phase of the storm, the ring current intensifies,

©2020. The Authors.

This is an open access article under the terms of the Creative Commons Attribution License, which permits use, distribution and reproduction in any medium, provided the original work is properly cited.

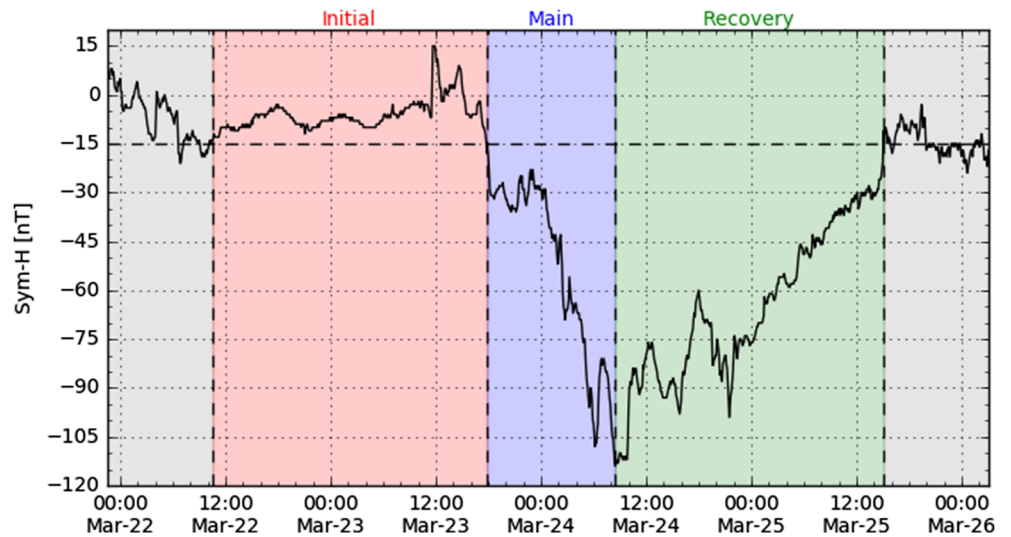


Figure 1. Illustration of the Sym-H algorithm on a storm from March 2002. The red section is the initial phase of the storm, the blue section is the main phase, and the green section is the recovery phase. An additional 12 hr of data has been shown in gray at either end of the storm interval.

which results in a sharp drop in the ring current index due to the weakened magnetic field. The recovery phase usually lasts several days as the ring current decays. Hence, a sharp decrease in the Sym-H index is indicative of a geomagnetic storm (e.g., Akasofu et al., 1963; Chapman & Ferraro, 1930).

Magnetic flux tubes, or field lines, can support standing Alfvén waves. The eigenfrequencies on any given flux tube depend upon the flux tube length, wave polarization, and the Alfvén speed v_A , which in turn depends on the magnetic field strength, B , and plasma mass density, ρ , of the flux tube (Cummings et al., 1969). The dependencies on v_A are given by

$$v_A = \frac{B}{\sqrt{\mu_0 \rho}} \quad (1)$$

where μ_0 is the permeability of free space. The eigenfrequencies of any given flux tube thus depend upon the relationship between these three parameters: Eigenfrequencies will increase if the magnetic field strength increases, the plasma mass density decreases, or the flux tube decreases in length.

1.1. Eigenfrequencies During Storm Times

Several studies have observed that the eigenfrequencies of closed magnetic field lines decrease as the ring current index decreases (becomes more negative). Wild et al. (2005) predicted this by using the time of flight technique to calculate eigenfrequencies in a T96 magnetic field model (Tsyganenko, 1996) parameterized by the Dst index. Sandhu, Yeoman, and Rae (2018) used the same technique but with the more realistic plasma mass density model of Sandhu et al. (2017) based on 12 years of Cluster data ($L > 5.9$) that could be parameterized by the Dst index and found the same result. Most recently, Wharton, Wright, Yeoman, James, et al. (2019) performed a statistical analysis of eigenfrequencies measured by the cross-phase technique applied to ground magnetometers and found that the eigenfrequencies decreased when the Sym-H index was reduced for $L > 4$.

Other studies have investigated single geomagnetic storm events. Kale et al. (2009), Takasaki, Kawano, et al. (2006), and Chi et al. (2005) all looked at the Halloween storm event in October 2003, and each found that the eigenfrequency decreased after a sudden storm commencement. Du et al. (2005) also found an eigenfrequency decrease for a storm in July 2000, Lee et al. (2007) for the March 1991 storm, and Rae et al. (2019) for the March 2013 storm. Warner and Orr (1979), Engebretson and Cahill Jr. (1981), and Takahashi et al. (2002) are among others to have observed eigenfrequencies decrease with increasing geomagnetic activity at the latitudes investigated in this study.

1.2. Corresponding Changes in Plasma Mass Density

The plasma mass density model of Sandhu et al. (2017) revealed that during periods of low Dst index, the plasma mass density decreased, despite the average ion mass increasing. This was because the electron

number density decreased. A reduced plasma mass density would increase the eigenfrequencies. However, Sandhu, Yeoman, and Rae (2018) used this model and the T96 magnetic field model to show that the eigenfrequencies decreased for low Dst values. This was because the reduction in the magnetic field strength created by an enhanced ring current was dominant in determining the eigenfrequencies over the reduced plasma mass density. Several other studies have shown that the plasma mass density decreases during enhanced geomagnetic activity (e.g., Corpo et al., 2018; Dent et al., 2006; Denton et al., 2006; Menk et al., 2014).

However, it has also been shown that the plasma mass density increases in response to increased geomagnetic activity (Takahashi et al., 2002, 2010; Takahashi, Denton, et al., 2006), and Min et al. (2013) showed that the plasma mass density barely changes. Chi et al. (2005), Takasaki, Kawano, et al. (2006), and Kale et al. (2009) also determined that the plasma mass density increased after the sudden storm commencement. Equation 1 shows that if the plasma mass density increases, then changes in both the plasma mass density and magnetic field strength are acting in cooperation to decrease the eigenfrequencies by reducing the Alfvén speed. In this scenario, just considering the change in magnetic field strength would not fully account for the decrease in eigenfrequency.

1.3. The Objectives of This Study

Studies based on correlating eigenfrequencies with a ring current index (e.g., Sandhu et al., 2017; Wharton, Wright, Yeoman, James, et al., 2019) do not fully capture the eigenfrequency evolution throughout a geomagnetic storm's three phases. Eigenfrequency data taken during the main and recovery phases will be combined when binning by only the value of a ring current index. For example, a bin containing all samples taken when the Dst index was -80 nT would include samples corresponding to both the main and recovery phases of a storm. It is important to consider the phases separately as each storm phase is associated with different magnetospheric processes. The statistics will also be dominated by data in the recovery phase, as this is typically the longest phase. Hence, the results will not typically describe what is happening in the main phase of the storm.

Other studies have looked at how the eigenfrequencies vary for specific storms (e.g., Lee et al., 2007; Rae et al., 2019) to explore the time evolution. However, these studies do not provide information on whether the storms are representative of the statistically average storm, especially as these studies focussed on more extreme events. Any storm related trends in the data will also be contaminated by diurnal effects. For example, if observations beginning in the morning observe an eigenfrequency decrease throughout the day as a storm is progressing, it is difficult to determine how much of this decrease is due to the storm and how much is due to the expected diurnal variation for a single event. The eigenfrequencies normally decrease when moving into the afternoon sector (e.g., Chappell et al., 1971; Chi et al., 2013; Sandhu, Yeoman, James, et al., 2018; Wharton, Wright, Yeoman, James, et al., 2019). Data from multiple storms are required to disentangle these two factors influencing the change in eigenfrequency.

A statistical study of a large number of storms enables us to determine the average trends in eigenfrequencies during storms and to reduce the diurnal variation. One hundred and thirty-two storms are identified using the algorithm of Walach and Grocott (2019). The cross-phase technique of Wharton et al. (2018), and Wharton, Wright, Yeoman, and Reimer (2019) is used to measure the eigenfrequencies, and the superposed multiple-epoch analysis method employed by Hutchinson et al. (2011) is used to find the average variation for all the storms. By multiple epoch, we mean that we have analyzed the initial, main, and recovery phases of the storm independently. This is the first reported study to employ a superposed epoch analysis to investigate the eigenfrequencies in cross-phase spectra. The superposed epoch analysis also puts all of the storms onto a common time grid so we can see how the average eigenfrequency varies relative to the storm phase and it prevents data from different storm phases being mixed together. By only including data in the analysis from a given magnetic local time (MLT) sector, the diurnal variation can be removed from the average. Different MLT sectors can then be analyzed separately. A chain of magnetometer stations allows us to investigate changes in eigenfrequency for different latitudes as well as MLTs.

Previous studies have provided a valuable understanding of how mass density changes. However, due to varying instrument coverage between studies, differing techniques, and limitations of the methodology as discussed earlier, the typical storm time variations are inconclusive with reports of both enhanced mass density and depletions of mass density during geomagnetic storms. We use our data to determine whether the plasma mass density increases or decreases for the average geomagnetic storm by solving the wave equation

Table 1
Locations of the Magnetometer Pairs

| Magnetometers | Identity code | Midpoint | Midpoint | Midpoint | Midpoint | L-shell |
|----------------------|---------------|----------|----------|----------|----------|---------|
| | | geo lat. | geo lon. | CGM lat. | CGM lon. | |
| Masi-Sorøya | MAS-SOR | 68.50 | 22.96 | 66.76 | 106.30 | 6.42 |
| Ivalo-Kevo | IVA-KEV | 69.16 | 27.15 | 65.71 | 108.91 | 5.91 |
| Pello-Muonio | PEL-MUO | 67.46 | 23.81 | 64.14 | 105.07 | 5.25 |
| Oulujärvi-Pello | OIJ-PEL | 65.71 | 25.66 | 62.27 | 105.53 | 4.62 |
| Hankasalmi-Oulujärvi | HAN-OIJ | 63.39 | 26.92 | 59.84 | 105.34 | 3.96 |
| Tartu-Nurmijärvi | TAR-NUR | 59.38 | 25.56 | 55.68 | 102.54 | 3.15 |

Note. Magnetic coordinates and dipolar L-shells are based on positions in 2001 (see <https://space.fmi.fi/image/www/index.php?page=stations>). These values vary slightly across the time range of the study.

of Singer et al. (1981) in conjunction with the TS05 magnetic field model (Tsyganenko & Sitnov, 2005). It is found that whether the plasma mass density increases or decreases depends on the L-shell observed.

2. Data

2.1. Geomagnetic Storm Intervals

To study the average changes in eigenfrequencies during geomagnetic storms, we have used a storm list created using the method of Walach and Grocott (2019). Their algorithm provides times that mark the four boundaries associated with the three phases mentioned in Section 1: initial, main, and recovery.

This algorithm searches the Sym-H index for minima less than -80 nT. This is the same criteria employed by Hutchinson et al. (2011). Some weak storms may have a Sym-H minimum greater than -80 nT, but it was deemed best to remove these to ensure that the minimum was due to a geomagnetic storm. This minimum defines the time at the end of the main phase. An example of this procedure is illustrated in Figure 1. The beginning of the main phase is defined as the most recent time before the Sym-H minimum crossed the quiet time level of -15 nT. Walach and Grocott (2019) found that this was a more reliable definition than using the preceding maximum Sym-H value. To define the beginning of the initial phase, the maximum value of Sym-H before the beginning of the main phase is identified. The most recent time before this when Sym-H is -15 nT is the beginning of the initial phase. Note that this definition of the start of the initial phase is different to that of Hutchinson et al. (2011) and Murphy et al. (2018), who use a definition based on dynamic pressure enhancements. The end of the recovery phase is defined as the next time after the end of the main phase when the Sym-H index returns to -15 nT. This algorithm is also discussed in Walach and Grocott (2019), where the list is used to investigate geomagnetic storms with the Super Dual Auroral Radar Network (Chisham et al., 2007; Greenwald et al., 1995) from 2010 to 2016.

This algorithm was applied to Sym-H data from 2002 to the end of 2018. After visually checking for false detections, this gave a list of 132 storms. The dates and Sym-H minima associated with each storm are given in the supporting information.

2.2. Magnetometer Data

This study used 10-s resolution magnetometer data from the International Monitor for Auroral and Geomagnetic Effects (IMAGE) array (Luhr, 1994). North-south component data from the stations listed in Table 1 were used in the analysis, which corresponds to the toroidal mode if we assume a 90° rotation of the wave ellipse by the ionosphere (Hughes & Southwood, 1976). Midpoint dipolar L-shell values are given to help visualize the latitudinal coverage of the pairs used in this study.

3. Cross-Phase Superposed Epoch Analysis

To investigate how the eigenfrequencies of magnetic field lines change during geomagnetic storms, a different approach was used to that of Wharton, Wright, Yeoman, James, et al. (2019). They simply binned measurements according to their Sym-H value. However, the Sym-H index only reaches storm levels, here defined as $\text{Sym-H} < -80$ nT, for a very small fraction of the total time available. Data from both the main and recovery phases will also be combined together, and no information about how the eigenfrequencies

evolve with time will be available. Therefore, we have taken a different approach by applying a superposed multiple-epoch analysis to the cross-phase spectra taken during the storm intervals identified with the method of Walach and Grocott (2019) described in Section 2.

The eigenfrequencies were determined using the cross-phase technique of Waters et al. (1991), which requires two latitudinally and closely spaced ground-based magnetometers. Two are required to detect the phase change with latitude that occurs at the resonant frequency of the midpoint of the magnetometers. Several papers have automated this technique (Berube et al., 2003; Chi et al., 2013; Sandhu, Yeoman, James, et al., 2018; Wharton et al., 2018).

Further to this, Wharton, Wright, Yeoman, and Reimer (2019) developed a Lomb-Scargle (LS) cross-phase technique that could process unevenly spaced data and use a higher frequency resolution because the frequency grid is independent of the properties of the data used. The chosen resolution was 4 times that achievable with a discrete Fourier transform as this value was adopted in previous studies which used LS (e.g., Bland et al., 2014; Wharton, Wright, Yeoman, James, et al., 2019; Wharton, Wright, Yeoman, & Reimer, 2019). The dynamic cross-phase spectrum uses a 40-min sliding window, which gives a frequency resolution of 0.417 mHz without oversampling for the IMAGE magnetometer resolution. Changing the oversampling factor to 4 reduces the frequency resolution to 0.104 mHz, allowing us to be more precise in determining the frequencies of waves. The LS technique is not intrinsically more accurate than using the discrete Fourier transform, but it does allow us to create a denser frequency axis. This was the motivation for using it in this paper.

The superposed multiple-epoch analysis method used by Hutchinson et al. (2011) was then applied to the derived cross-phase spectra. This method treats the three phases of geomagnetic storms separately by calculating the mean duration of each of the three storm phases (initial, main, and recovery). A superposed epoch analysis is then applied to each storm phase. This method is better than applying a superposed epoch analysis to the whole storm interval because the durations of each phase are not always in the same proportion to each other for different storms. Treating the three phases independently accounts for this. These mean durations were 33.16, 11.76, and 53.10 hr for the initial, main, and recovery phases, respectively. This enabled us to create a common time grid to which the three phases of each storm could be normalized to so we could observe average changes in each of the three storm phases.

For each storm, the LS cross-phase spectrum was calculated. Figure 2 shows an example of how the rescaling was performed on one of the storm intervals. Figure 2a contains the filtered magnetometer data (800-s boxcar filter (Wharton et al., 2018)) for two magnetometer stations. Figure 2b shows the LS cross-phase spectrum for this storm. The initial, main, and recovery phases have been shaded red, blue, and green, respectively. An additional 12 hr of data has been included on each end, shaded in gray, to represent the quiet time periods and will be used to compare variations to quiet time conditions.

Before the rescaling and averaging process could be performed, there is a complication concerned with MLT that had to be considered. The full duration of a geomagnetic storm is usually a few days. This means that the diurnal variation of the eigenfrequencies must be taken into account. For example, eigenfrequencies are always higher in the morning sector than the afternoon (e.g., Takahashi et al., 2016; Wharton et al., 2018). This is because the plasma mass density is higher in the afternoon sector relative to the morning due to flux tubes refilling from the ionosphere throughout the day. If this is not accounted for, changes in the eigenfrequencies that are diurnal and storm related will be mixed together. To compensate for this, a MLT sector is first defined (e.g., 10–14). We arbitrarily chose 4 hr as a compromise between minimizing diurnal variability and not excluding too much data. Only data taken when the magnetometer pair were within that MLT sector were included in the superposed epoch analysis described above. The analysis was then performed independently for other MLT sectors. This minimized contamination of the spectra by diurnal variation so that only the storm-related variations were observed.

To perform the superposed epoch analysis, each frequency in the periodogram was treated as its own time series. Each “frequency time series” was interpolated and then rescaled to the common time axis for each phase of the storm. This gave the rescaled LS cross-phase spectrum in Figure 2c. This process was repeated for all storms so that the spectra could then be superposed and averaged using the common time grid. In this example, data from all 24 hr of MLT have been included to more clearly show the rescaling process. For the

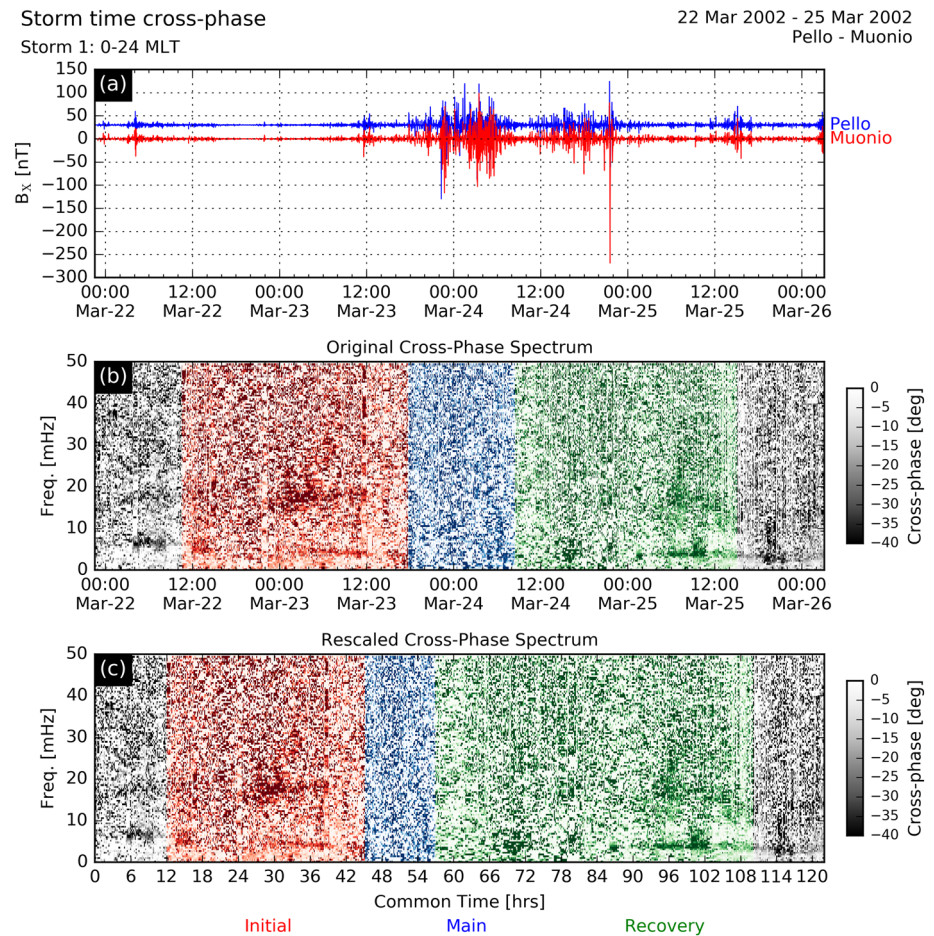


Figure 2. Rescaling of cross-phase spectra. (a) Boxcar filtered magnetometer data for the two stations. (b) Original LS cross-phase spectrum. Initial phase: red. Main phase: blue. Recovery phase: green. (c) Cross-phase spectrum rescaled to the common time axis using the method of Hutchinson et al. (2011).

forthcoming analysis, only data taken from 4-hr MLT sectors are included. The equivalent plot here would contain considerable white space due to the excluded data.

The superposed multiple-epoch analysis method used by Hutchinson et al. (2011) was also applied to variables from the OMNI data set, which describes the upstream solar wind and contains geomagnetic indices. This is shown for the Sym-H index in Figure 3a, where the three phases of the storm have the same color (red, blue, and green). The mean, median, and upper and lower quartiles of the Sym-H index have been overlotted.

Figure 3 gives an example of the superposed epoch analysis applied to the 132 storms for the Pello-Muonio magnetometer pair in the 10–14 MLT sector. Figure 3b shows the number of storms that contributed data to each time on the common time axis. This number varies because the storms were not equally distributed in MLT. On average, 22 storms were expected at any given time due to the size of the MLT sector.

Figure 3c shows the results of the superposed epoch analysis on the LS cross-phase spectra taken in the 10–14 MLT sector for all 132 storms. The LS cross-phase spectra for all of the storms have been circularly averaged in each frequency—common time bin because the cross phase is a circularly distributed variable (Mardia & Jupp, 2000). A variation in the fundamental eigenfrequency is visible. The trend is least clear in the initial phase but begins at ~ 8 mHz at the beginning of the phase and reaches ~ 4 mHz at the start of the main phase. Other bands can also be seen at higher frequencies, which complicates the interpretation of the harmonic numbers. The eigenfrequency reaches a minimum at ~ 4 mHz in the main phase, where it remains steady before increasing again throughout the recovery phase back to 8 mHz. Only the fundamental was observable in the recovery phase.

Average storm time cross-phase: 10-14 MLT

132 storms
PEL - MUO: L = 5.21

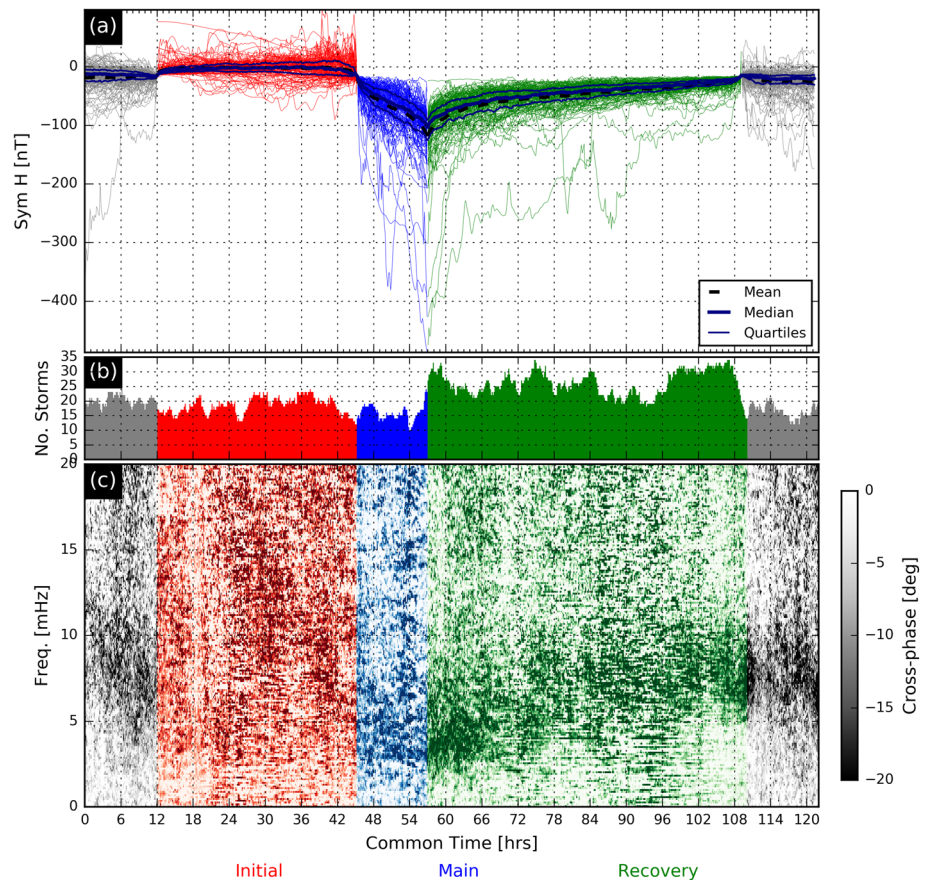


Figure 3. Superposed multiple-epoch analysis results for the Pello-Muonio station pair in the 10–14 MLT window. (a) Superposed multiple-epoch analysis on the Sym-H data. The dashed line shows the mean Sym-H value, the thick solid line shows the median, and the thin solid lines show the upper and lower quartiles. (b) The number of storms contributing to the average as a function of common time. (c) Superposed multiple-epoch analysis of the LS cross-phase spectra. Red shading indicates initial phase, blue is main phase, and green is recovery phase. Gray is 12 hr before and after the storm.

Identifying the fundamental eigenfrequency in the initial phase is ambiguous and complicated by the possible presence of a higher harmonic. This could be the third harmonic, based on the arguments in Wharton et al. (2018), and it also decreases in value toward the main phase from ~ 15 to ~ 5 mHz. It could also be the fundamental eigenfrequency increasing around 24 hr then decreasing again. The selection algorithm in Section 4.1 tries to address this ambiguity with a manual process.

The same analysis was performed for the other station pairs at the latitudes given in Table 1. Although there were some differences in whether the third or fundamental harmonic were being observed during the initial phase, a consistent pattern of decreasing eigenfrequencies was observed at all but the lowest latitudes. This decrease in eigenfrequency with increasingly negative Sym-H is in agreement with observations by Sandhu, Yeoman, and Rae (2018) and Wharton, Wright, Yeoman, James, et al. (2019). Other latitudes and MLTs are presented in the next section, and the results will be summarized in Figures 6 and 7, which separate out the storm time and diurnal variation.

4. Controlling Factors for the Eigenfrequency

Changes in the eigenfrequency values depend on the magnetic field structure and plasma mass density, as discussed in Section 1. Calculating the average changes in these parameters allows an understanding of why the eigenfrequencies vary throughout the storm cycle. To do this, a range of appropriate frequencies centered on the eigenfrequency must be extracted from the data and expressed as a function of the common

Average storm time cross-phase: 10-14 MLT
Averaging Box: 4.0 mHz - 4.0 hrs

132 storms
Pello - Muonio

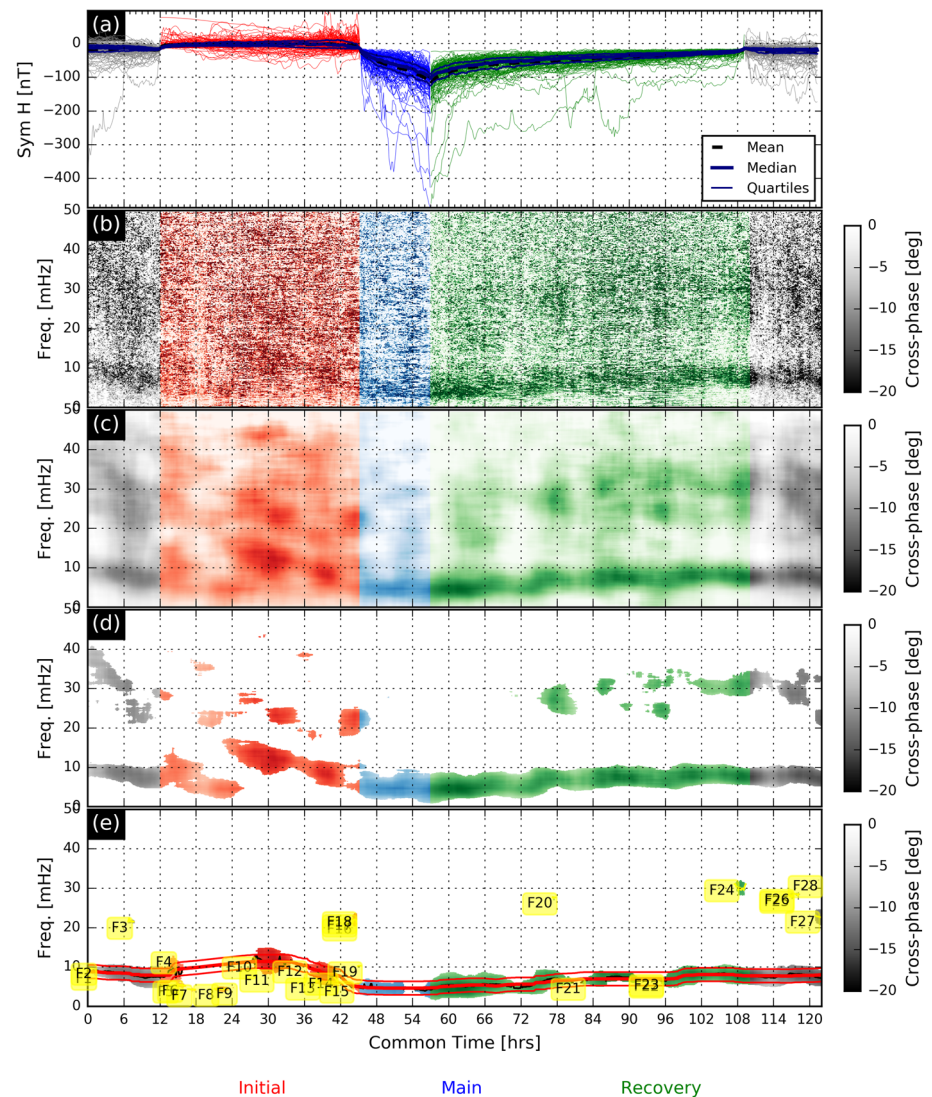


Figure 4. Procedure for isolating the fundamental frequency. (a) Superposed epoch analysis results on the Sym-H index data. (b) Average LS cross-phase spectrum. (c) Smoothed, average LS cross-phase spectrum. (d) Smoothed spectrum after column test. Only values less than the column mean minus one standard deviation are kept. (e) Spectrum after the t test. Only cross-phase values with a t statistic greater than 1 remain. Each independent feature is identified and labeled (yellow). “F” stands for feature and the number corresponds to the order in which they were identified. Features thought to contribute to the fundamental are selected and a line is fitted through them and smoothed (thick red line). Thin red lines indicate the uncertainty in the eigenfrequency described in the text.

time axis to enable calculation. This is difficult using the data in the format displayed in Figure 3. Section 4.1 describes this extraction process. In Section 4.2, we parameterize the TS05 magnetic field model (Tsyganenko & Sitnov, 2005) and calculate the plasma mass density. In Section 4.3, we repeat this for all station pairs in Table 1 and for a range of MLTs. This enables the derivation of eigenfrequency maps and, by accounting for magnetic field changes according to the TS05 model, estimations of equatorial plasma mass density. The results provide a fuller understanding of how the structure of the dayside magnetosphere changes during geomagnetic storms, at least within the region covered by the magnetometers in this study.

4.1. Isolating the Fundamental Eigenfrequency

The technique to extract the fundamental eigenfrequency profile is based on that of Wharton et al. (2018) with an additional step, which is illustrated in Figure 4. Figures 4a and 4b are reproduced directly from

Figure 3. The LS cross-phase spectrum is first smoothed in both time and frequency (Figure 4c). To do this for any given value, it is averaged with values within ± 2 mHz and ± 2 hr, giving a range or box size of 4 mHz by 4 hr. At the edges of the spectrum, these ranges will be capped by the spectrum boundaries (0 or 50 mHz for frequency and the start and end times), shrinking these ranges to half their size for the boundary values. Hence, the standard error will be larger at the plot boundaries. The standard deviation is also calculated and stored for the purposes of the t test explained below.

Next, the mean and standard deviation of the cross phase for each common time are calculated. Only values less than the mean minus one standard deviation are retained. The result of this is illustrated in Figure 4d. It can be seen that a narrow frequency band where the fundamental frequency lies dominates the remaining data. Then a t test is applied to remove the nonresonant features. The statistic is the smoothed cross-phase value divided by its standard deviation and multiplied by minus 1. Only cross-phase values with a t statistic greater than one are kept. Nonresonant signatures randomly had a highly negative cross-phase value, but their large standard deviation can be used to remove them. Only the stable values then remain, which are presumed to represent real eigenfrequencies. This process is also discussed in Berube et al. (2003), the algorithm upon which the Wharton et al. (2018) algorithm was originally based. These are shown in Figure 4e.

We then use a process that searches through the spectrum and isolates the remaining independent features and assigns them a number. This process searches up each column in Figure 4d, beginning at the bottom left, until it finds a data point. It then searches this column and adjacent columns for data in adjacent cells and groups this data together. This group is a feature, and these data are then discounted from the rest of the search. Once all points that are grouped together are found, the search up the columns continues looking for the start of the next feature and so forth. The final list of identified features is labeled with the numbers in the yellow boxes in Figure 4e that are automatically attached to their respective features. “F” stands for feature and the number corresponds to the order in which they were identified. Hence, lower numbers are to the left where the search began. The user can then manually select which “features” they think contribute to the fundamental eigenfrequency. This is a subjective process to a certain extent. In some cases, the labels overlap because two features begin in very similar locations on the plot. In such circumstances, trial and error is unfortunately required to select the desired features. For the example in Figure 4e, the features 1, 2, 10, 12, 15, 21, 22, and 23 were selected by the user. These features are then fitted with a smooth line to yield an eigenfrequency profile, which is the thick red line in Figure 4e.

The band identified in Figure 4e is spread over a range of frequencies. An uncertainty on the eigenfrequency is found by calculating the mean frequency width of the selected features that composed the fundamental eigenfrequency. This range is illustrated by the two thin red lines in Figure 4e and represents an estimate in the uncertainty in measuring the fundamental frequency using this method.

This method was considered more reliable than employing a complicated automated algorithm. The primary issue is that there are often multiple harmonics, which could contaminate the fundamental, so automatic identification becomes difficult. This method was a way of resolving this problem. It is noted that advanced machine learning methods could be applied in future but such methods were not needed for the small number of cases in this study.

4.2. Determining the Plasma Mass Density

Once the fundamental frequency has been determined as a function of the common time as described in Section 4.1, the next step is to describe the magnetic field line. Once achieved, the magnetohydrodynamic (MHD) wave equation of Singer et al. (1981), Equation 2, can be solved to determine the plasma mass density.

We chose the TS05 magnetic field model (Tsyganenko & Sitnov, 2005) to model the magnetic field lines, which was designed to include the variability introduced by geomagnetic storms and specifically includes a ring current contribution. Huang et al. (2008) have shown that the performance of this model is better than previous empirical magnetic field models. The parameters for this model are the Dst index (we have used the Sym-H index, which can be considered as a high resolution Dst index (Wanliss & Showalter, 2006)), solar wind dynamic pressure and velocity, IMF x and y components and the dipole tilt angle.

To parameterize the TS05 model across the common time axis, the superposed multiple-epoch analysis method described in Section 3 was applied to the Sym-H, pressure, IMF B_z , and solar wind velocity x component data. This process is illustrated in Figure 5 for the Pello-Muonio pair in the 10–14 MLT sector. The

Average storm time cross-phase: 10-14 MLT

132 storms
Pello - Muonio
L = 5.21

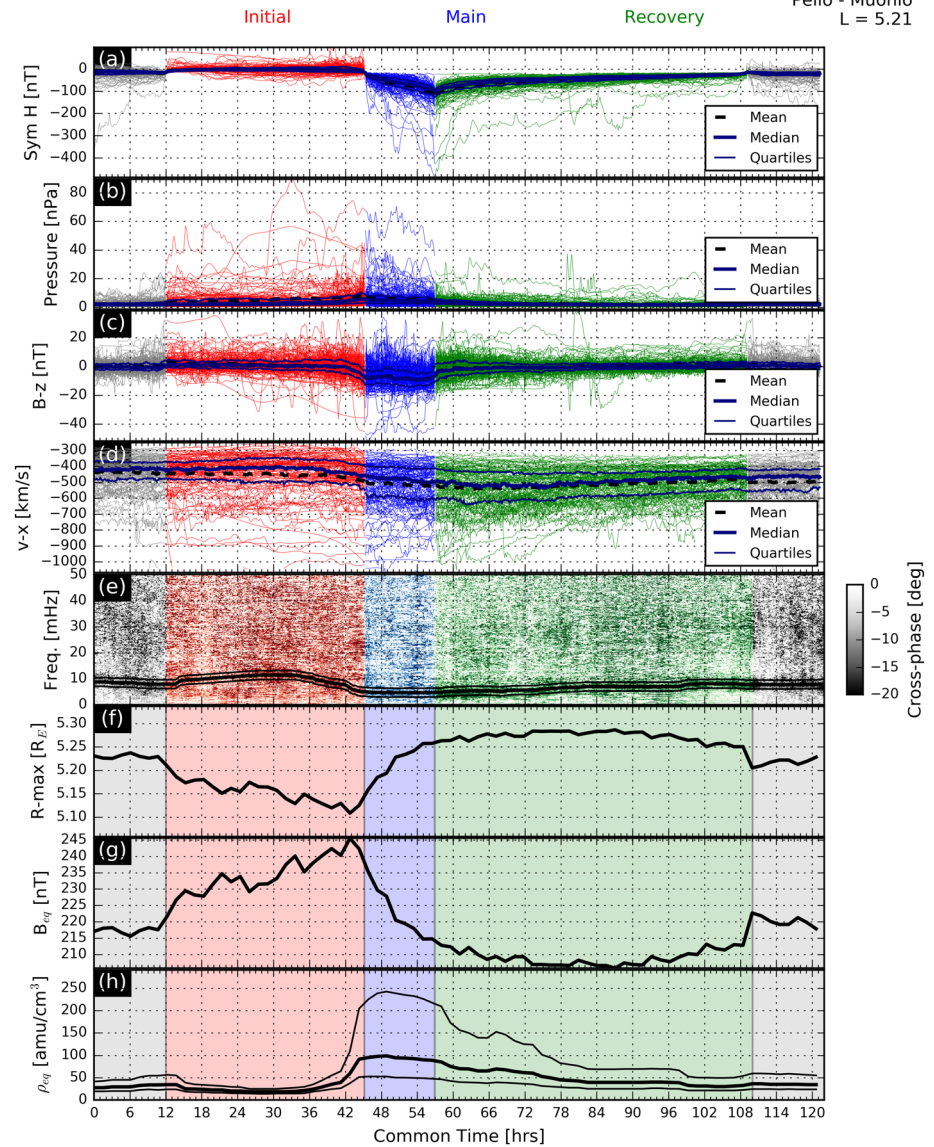


Figure 5. Process to retrieve magnetic field and plasma mass density information. Superposed multiple-epoch analyses for (a) Sym-H index, (b) solar wind dynamic pressure, (c) IMF B_z component, and (d) solar wind velocity v_x component. (e) Superposed epoch analysis LS cross-phase spectrum with fundamental eigenfrequency profile overplotted. (f) Radial position of the magnetic field line for this magnetometer pair according to the TS05 model. (g) Equatorial magnetic field strength. (h) Equatorial plasma mass density. The thicker line is for the middle eigenfrequency profile, and the thinner lines correspond to the upper and lower eigenfrequency bounds.

superposed epoch analysis of the Sym-H, dynamic pressure, IMF B_z , and solar wind velocity x component data are shown in Figures 5a–5d. The mean values of these four parameters at each common time were used for parameterizing the TS05 model. The solar wind velocity y and z components, dipole tilt angle, and IMF B_y data were all set to 0, as this was their expected average values. Over long time scales, the solar wind flow is expected to be radial and the dipole tilt angle will average to 0. Therefore, the IMF B_y component should not affect the storm process either. This was confirmed from applying the superposed epoch analysis method to these variables to check. The superposed epoch analysis cross spectrum from Figure 3b is reproduced in Figure 5e with the eigenfrequency profile from Figure 4e plotted over it.

The TS05 model was evaluated for every tenth point available on the common time axis. Figure 5f shows the maximum radial distance of any point along the field line, assumed to represent the equatorial crossing

point. As the initial phase begins, the field line moves earthward until the main phase, where it then moves outward beyond its original position. The field lines recover toward their original position at the end of the recovery phase.

Plotted in Figure 5g is the magnetic field strength at the maximum radial distance of the field line. Note that in the equatorial plane, the magnetic field strength is primarily dominated by the B_z component. This is observed to increase throughout the initial phase as the magnetopause currents are enhanced and the closed magnetic field line strength increases, then drops throughout the main phase as the enhanced ring current weakens the background magnetic field. It then returns to normal during the recovery phase. These results show that the TS05 model is capturing the expected aspects of a geomagnetic storm.

The MHD wave equation, derived by Singer et al. (1981),

$$\frac{d^2}{ds^2} \left(\frac{\epsilon_\alpha}{h_\alpha} \right) + \frac{d}{ds} \left(\ln(h_\alpha^2 B_0) \right) \frac{d}{ds} \left(\frac{\epsilon_\alpha}{h_\alpha} \right) + \frac{\mu_0 \rho \omega^2}{B_0^2} \left(\frac{\epsilon_\alpha}{h_\alpha} \right) = 0 \quad (2)$$

has been used to calculate the equatorial plasma mass density. The justification for using this equation is given below. Solving this equation requires knowledge of the magnetic field structure and the eigenfrequency. We have used the TS05 magnetic field model and the eigenfrequencies measured from our data. In Equation 2, ϵ_α is the field line displacement, h_α is a scaling factor describing the separation of the field lines along the field, s is the field-aligned coordinate, B_0 is the ambient magnetic field strength, μ_0 is the magnetic permeability of free space, ω is the angular eigenfrequency, and ρ is the plasma mass density. The separation h_α is calculated in the toroidal direction using a closely spaced field line.

Singer et al. (1981) state that Equation 2 can be applied to any arbitrary geometry. The derivation of this equation implicitly assumes that orthogonal field-aligned coordinates can be used. However, Salat and Tataronis (2000) have shown that such fields only exist in special cases, such as a dipolar field. In general, fields that can support field-aligned orthogonal coordinates do not exist and this includes the TS05 fields. Using orthogonal coordinates requires $\mathbf{B} \cdot (\nabla \times \mathbf{B}) = 0$ or that there is no shear in the magnetic field. An absence of shear requires that the magnetic field is 0 in one of the three coordinate directions. In a dipole field, this would be the azimuthal direction. For a more realistic magnetospheric field line, there will be variation in the magnetic field in all three field-aligned coordinates due to shear, and thus, an orthogonal field-aligned coordinate system is not possible. Therefore, solving the wave equation in a nonorthogonal coordinate system such as that of Rankin et al. (2006) would be more accurate, despite the more complicated formulation of the wave equation. In this study though, we only consider magnetic field lines in the dayside magnetosphere away from the magnetopause, which can be considered to be quasi-dipolar. Hence, any error from using Equation 2 is expected to be minimal, and many other authors have used this equation when tackling this problem (e.g., Berube et al., 2006; Waters et al., 1996; Wharton et al., 2018). Therefore, we have applied this equation to our problem.

Equation 2 is solved using the Runge-Kutta method described in Wharton et al. (2018). The plasma mass density is assumed to have the power law form for its distribution along the field line given by

$$\rho = \rho_{eq} \left(\frac{r_{eq}}{r} \right)^3 \quad (3)$$

This is a common assumption made by many authors (e.g., Angerami & Thomas, 1964; Carpenter & Smith, 1964; Cummings et al., 1969; Denton et al., 2006; Menk et al., 1999, 2004; Orr & Matthew, 1971; Wharton et al., 2018). In Equation 3, ρ is the plasma mass density and r is the radial position along the field line. The subscript *eq* represents the equatorial value. The exponent determines the rate at which the plasma mass density changes with radial distance. A positive exponent causes the plasma mass density to decrease radially, so that it reaches a minimum along a field line in the equatorial plane. An exponent of 3 has been used, and it is assumed this is a reasonable value based on other studies and has been used by many other authors (e.g., Poulter et al., 1984; Menk et al., 1999, 2004). This distribution contains a minimum at the equator and maxima at the base of the field lines in the ionosphere. The size of this exponent has been shown to make little difference to the calculated equatorial mass densities (e.g., Menk & Waters, 2013; Orr & Matthew, 1971).

The equatorial plasma mass density profiles calculated with the mean fundamental frequency and the upper and lower bounds are shown in Figure 5h. The lower bound eigenfrequency corresponds to the highest

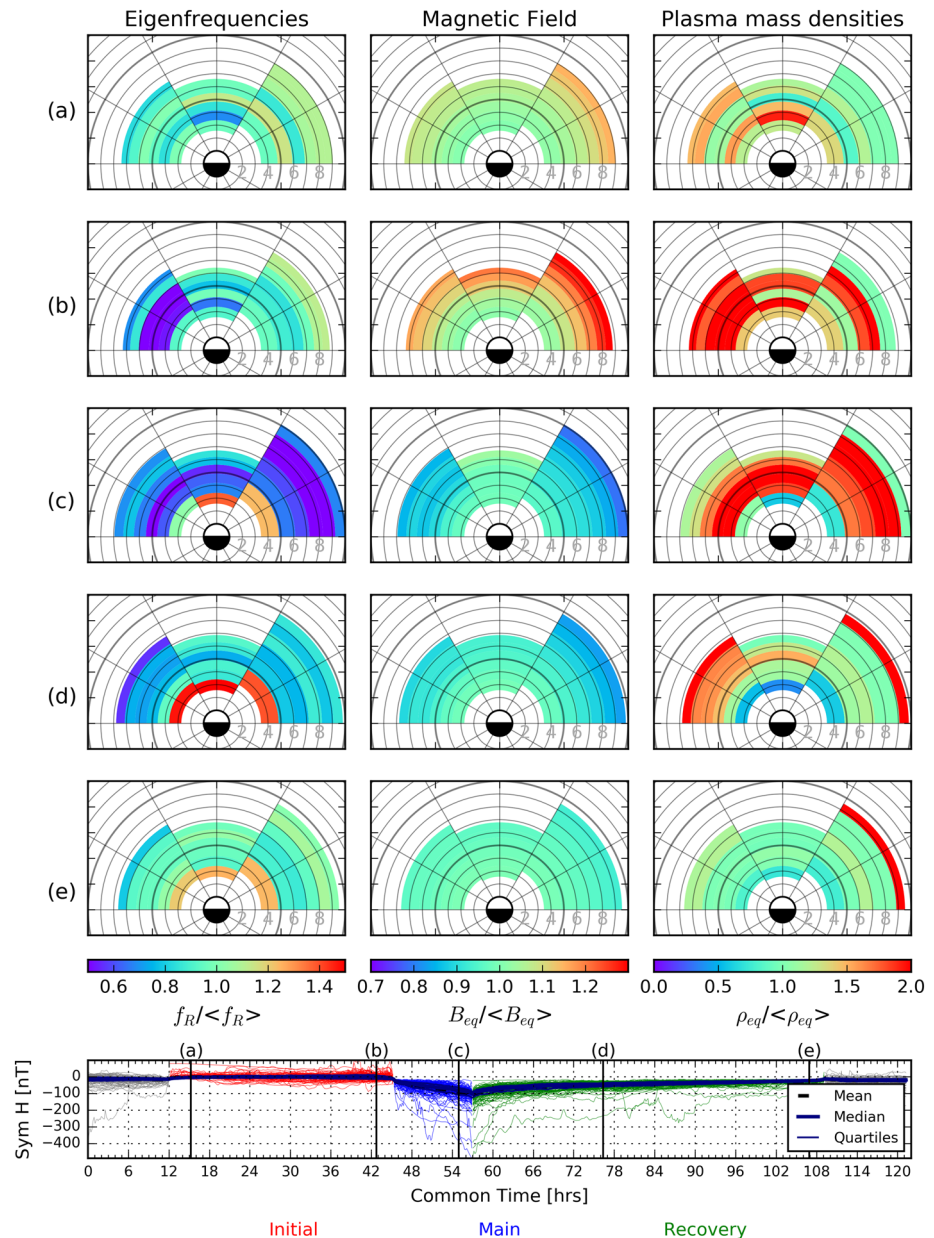


Figure 6. (a–e) Variations of measured eigenfrequencies, modeled equatorial magnetic field strengths, and calculated equatorial plasma mass densities relative to the local quiet time averages. (left column) Eigenfrequencies. (middle column) Magnetic field strength. (right column) Plasma mass densities. Each row shows the magnetospheric state at five intervals during the average geomagnetic storm, marked on the Sym-H index plot at the bottom.

plasma density and vice versa. In this example, the plasma density remains stable throughout the initial phase, which could suggest that as the magnetosphere is compressed, that plasma loss processes increase. The plasma mass density then increases to its highest value at the beginning of the main phase. It then decreases back to quiet time levels throughout the recovery phase. Small differences in the eigenfrequency correspond to large differences in the calculated plasma mass densities, in agreement with previous studies (e.g., Takahashi & Denton, 2007).

4.3. Mapping the Plasma Mass Density

The process of estimating the equatorial mass density described in Section 4.2 was repeated for each station pair in Table 1 for three MLT sectors, 6–10, 10–14, and 14–18 MLT. Only the dayside was considered because the cross-phase technique is ineffective at night (e.g., Wharton, Wright, Yeoman, James, et al., 2019). There

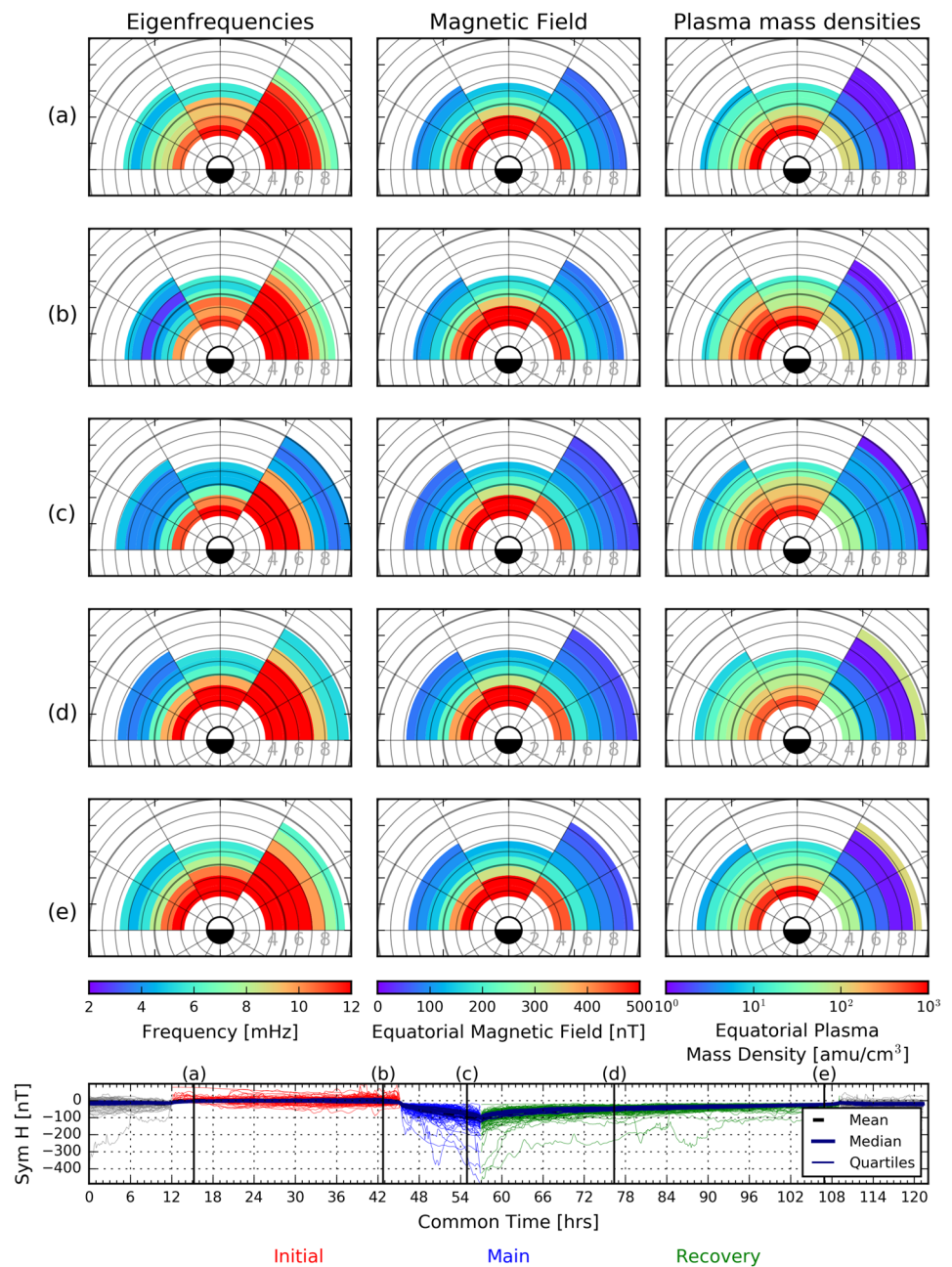


Figure 7. (a–e) Absolute variations of eigenfrequencies, equatorial magnetic field strengths, and equatorial plasma mass densities. (left column) Eigenfrequencies. (middle column) Magnetic field strength. (right column) Plasma mass densities. Each row shows the magnetospheric state at five intervals during the average geomagnetic storm, marked on the Sym-H index plot at the bottom.

was considerable variation in the plasma mass density profiles between different stations and MLTs. These results have been summarized by the maps in Figure 6, similar to those created in Corpo et al. (2018) using data from the European Meridional Magnetometer Array and parameterized by Kp index. The fundamental eigenfrequency measured with the LS cross-phase technique in Section 4.1, the modeled equatorial magnetic field strength from the TS05 model, and the inferred equatorial plasma mass densities, both from Section 4.2, are shown for each radial position and MLT sector for five intervals along the common time axis. These five times are labeled (a) to (e) and are indicated on the Sym-H index plot at the bottom. The TS05 model was used to map the field line of each station pair to the equatorial plane for each point in time, which accounts for the variation in field line length as the storms progress. The eigenfrequency data are shown on the left,

equatorial magnetic field data in the middle, and equatorial plasma mass density data on the right. Plots of the form of Figure 3 show that there are a sufficient number of storms in each MLT sector at all times to do this analysis.

For each MLT-radial bin, the quiet time average value of either the eigenfrequency, magnetic field strength, or plasma mass density is calculated from the 12-hr period before the initial phase and the 12-hr period after the recovery phase. These data are shaded in gray in Figures 1–5. This value is then used to normalize the respective data in that bin so we can see how the values change relative to their quiet time average. This approach made it much easier to discern the general trends as opposed to observing individual plots such as Figure 5. Each color scale is centered on 1. Hence, blue indicates a reduction in that value, and red an increase relative to quiet times.

An equivalent plot with absolute eigenfrequency, equatorial magnetic field, and plasma mass density values is shown in Figure 7 in the same format as Figure 6. This shows that the variation in eigenfrequency with L-shell and MLT is much greater than the storm time variation at any given position, making such variations difficult to discern. Hence, we focus our discussion on the normalized data in Figure 6. Here, an L value refers to the radial distance in the equatorial plane to the field line in Earth radii.

Figure 6a shows the beginning of the initial phase, when values are near the quiet time average. Figure 6b shows the end of the initial phase, where the eigenfrequencies have decreased in the 14–18 MLT sector and the magnetic field strength has increased for the outer L-shells. There has also been an increase in the plasma mass density, mostly clearly in the afternoon sector.

Figure 6c shows the end of the main phase. The eigenfrequencies have decreased by as much as 50% across most L-shells and MLTs. At the innermost L-shells, the eigenfrequencies are actually greater than the local quiet time average. The magnetic field has weakened, especially in the 6–10 and 14–18 MLT sectors. The plasma mass density has also increased across all sectors, except at the innermost L-shells where the opposite is observed.

Figure 6d shows partway through the recovery phase. The eigenfrequencies have risen back toward mean levels again but at the innermost L-shells, they are still higher than during quiet times. The magnetic field is still weaker than during quiet times. The plasma mass density has decreased again and remains above average only at the outermost L-shells. It is still below average at the inner distances. Finally, Figure 6e shows the end of the recovery phase, where for the most part, all three parameters have returned back to their quiet time averages.

5. Discussion

Based upon this analysis, Figure 6 demonstrates that there is a clear pattern in the behavior of measured toroidal eigenfrequencies during an average geomagnetic storm. The Alfvén speed, and hence a given field line eigenfrequency, is proportional to the magnetic field strength and inversely proportional to the square root of the plasma mass density (Equation 1). Hence, understanding both the field line structure and the plasma mass density distribution is necessary to determine why any field line eigenfrequency changes with time.

Section 5.1 discusses the changes seen at $L > 4$ in the context of changing magnetic field strength and plasma mass densities. Section 5.2 then discusses changes observed for $L < 4$, which had different variations in eigenfrequency and plasma mass density.

5.1. Causes of the Variation in the Eigenfrequencies: $L > 4$

Figure 7 shows that during all phases of the storm, the eigenfrequencies are consistently greater in the morning sector than the afternoon sector, which is the same across all observed L-shells. With asymmetries in magnetic field configuration as described by the TS05 model removed, the asymmetry persists and consequently must be caused by plasma mass density asymmetry. This asymmetry in MLT is well documented (e.g., Poulter et al., 1984; Sandhu, Yeoman, James, et al., 2018; Takahashi & McPherron, 1984; Takahashi et al., 2016; Wharton et al., 2018; Wharton, Wright, Yeoman, James, et al., 2019), and we confirm that this asymmetry persists throughout all phases of a geomagnetic storm. The higher plasma mass densities in the afternoon lower the Alfvén speed in this sector. This extra plasma could be due to the existence of a plasmaspheric bulge, plasmaspheric plume, or increased refilling of ionospheric flux tubes. The average ion mass is

also greater in the afternoon sector due to convection of heavy ions from the nightside plasma sheet (Sandhu et al., 2016).

We now consider the storm time variations that occur for $L > 4$. Figure 6b shows the change that occurs during the initial phase. For $L > 4$, the eigenfrequencies first decrease in the afternoon sector, which corresponds with plasma mass density increases of approximately 100% in some cells. This change is also most prevalent at $L < 7$. At radial distances greater than this, the magnetic field has increased due to the enhanced magnetopause currents, which would increase the eigenfrequencies.

Changes during the main phase are shown in Figure 6c. Here, the eigenfrequencies have decreased by as much as 50% across all MLT sectors. This corresponds with a magnetic field decrease, most prevalent away from the noon sector where magnetospheric compression is strongest, and plasma mass density increases across all MLT sectors. The decrease in eigenfrequency during the main phase when the ring current index is low agrees with the observations by Chi et al. (2005), Takasaki, Kawano, et al. (2006), Kale et al. (2009), Sandhu, Yeoman, and Rae (2018), Wharton, Wright, Yeoman, James, et al. (2019), and Rae et al. (2019).

Figures 6d and 6e show that the eigenfrequencies recover back to their quiet time levels as the recovery phase progresses. The return to quiet time values takes longest in the afternoon sector. This may be due to the existence of a lasting plasmaspheric plume.

The storm time variation in the equatorial magnetic field strength is as expected, due to the increase of the ring current magnetic field. However, this study demonstrates that the role of the plasma mass densities in determining the storm time evolution of the eigenfrequencies is greater than previously thought by Sandhu, Yeoman, and Rae (2018) and Rae et al. (2019). Previous studies have differed about whether the plasma mass density increases or decreases during storms. Sandhu et al. (2017) found using an empirical model that the plasma mass density decreased during intervals of low Dst index, despite the average ion mass increasing. This was because the electron number density decreased due to increased magnetospheric convection. Several other studies have also put forward evidence that the plasma mass density decreases during enhanced geomagnetic activity (e.g., Dent et al., 2006; Denton et al., 2006; Corpo et al., 2018; Menk et al., 2014). However, there are other studies that have found the plasma mass density increases (e.g., Chi et al., 2005; Kale et al., 2009; Takahashi et al., 2002, 2010; Takasaki, Kawano, et al., 2006; Takahashi, Denton, et al., 2006), which agrees with our findings. This increase was attributed to an increasing average ion mass (e.g., Kronberg et al., 2014). We show that at distances of $L > 4$, the plasma mass density doubles during the main phase of the storm across the whole dayside MLT sector and a wide range of L-shells. This shows that the plasma mass density and the magnetic field change in cooperation instead of opposition to lower the eigenfrequencies.

Where does this extra plasma mass originate from during the geomagnetic storm? The density of the hot O^+ population has been shown to increase during the main phase for $L < 7$ (Yue et al., 2019), and the partial pressure contribution from O^+ can be as great as that of H^+ (e.g., Nosé et al., 2011; Mitani et al., 2019). A rise in the density of O^+ in the ring current could explain our observations of enhanced plasma mass density with lower magnetic field. The cold O^+ population is also thought to increase due to higher outflows on the nightside during storms (e.g., Gkioulidou et al., 2019; Kistler et al., 2016). However, it is not possible to determine from our data if these populations are responsible for the plasma mass density changes, and if so, which populations dominate. Investigating these changes is beyond the scope of this study.

From a theoretical viewpoint, the lower eigenfrequencies during storm times would allow fast mode waves of given frequency to couple to field lines deeper in the magnetosphere, where they would produce standing Alfvén waves through the field line resonance mechanism (e.g., Southwood, 1974). Figure 7 also shows that these locations would be deeper in the afternoon than the morning due to the magnetospheric asymmetry about noon. Single event case studies such as Lee et al. (2007) and Rae et al. (2019) show that decreased eigenfrequencies during storm times coincide with enhanced ultralow frequency (ULF) wave power across large regions in the inner magnetosphere. Although this study shows that lower eigenfrequencies at $L > 4$ are a consistent feature of geomagnetic storms, it does not provide measurements of ULF wave power. The decreased eigenfrequencies are expected to contribute to the increased ULF wave power due to the power law power distribution of ULF waves (e.g., Rae et al., 2012), but other factors may also play important roles including the initial power of the fast mode waves, their frequency spectrum, their azimuthal wave numbers, or changing ionospheric boundary conditions. Establishing the importance of and isolating the effect of decreased eigenfrequencies on ULF wave propagation will be the focus of a future study.

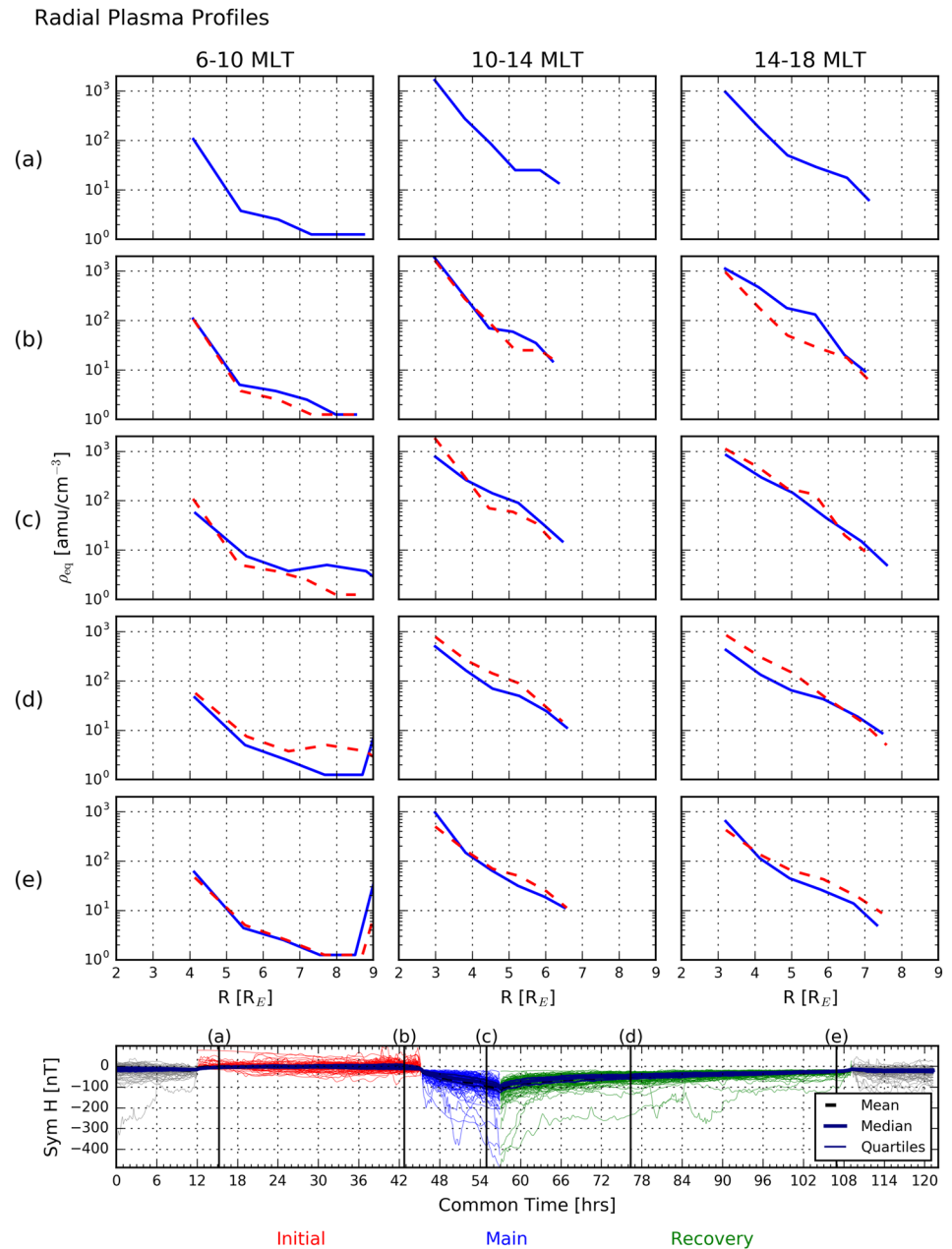


Figure 8. (a–e) The average plasma mass density at different phases of a geomagnetic storm. Each column represents data from the 6–10, 10–14, and 14–18 MLT sectors from left to right. Each row shows the magnetospheric state at five intervals during the average geomagnetic storm, marked on the Sym-H index plot at the bottom. Blue solid lines show the plasma mass densities at that interval of the storm, and red dashed lines show the previous interval for comparison.

5.2. Causes of the Variation in the Eigenfrequencies: $L < 4$

By including the Tartu-Nurmijärvi pair, changes within the plasmasphere have also been observed. Figure 6 shows that the eigenfrequencies and plasma mass densities had a different behavior on field lines where $L < 4$ than $L > 4$. Instead of decreasing, the eigenfrequencies increase, and the plasma mass densities decrease instead of increasing. The timing of this change is also delayed until the main phase, whereas changes for $L > 4$ begin during the initial phase. Relative to quiet time, the eigenfrequencies have increased by more than 50% partway through the recovery phase. The magnetic field change is much weaker for $L < 4$ compared to $L > 4$, suggesting that the reduced plasma mass density is almost entirely responsible for the increase in

eigenfrequencies. It also suggests that the effect of the ring current magnetic field is weaker for these inner shells. Figure 6d shows a decrease in plasma mass density of more than 50%.

During a geomagnetic storm, the plasmopause boundary is eroded away by the increased convection of the Dungey cycle and a plasmaspheric plume forms (e.g., Chappell et al., 1971; Menk et al., 2014). Regions that previously were within the plasmopause are now outside and have a much lower plasma mass density. This would increase the eigenfrequencies (Dent et al., 2006; Kale et al., 2007; Menk et al., 2004). It is difficult to say where the plasmopause is in Figure 6 or Figure 7. Figure 8 shows the plasma mass density data from Figure 7 as radial profiles. Each column represents one of the three MLT sectors, and each row a point along the storm time axis shown at the bottom, the same as in Figures 6 and 7. The blue line shows the plasma mass density profile at that time, and the dashed red line is from the time/row before to help show how the plasma mass density has changed. If there is a consistent location for the plasmopause during all storms, it would be visible as a classic “knee” in this plot but because these data show the average values of 132 storms, there is likely to be considerable variation in the plasmopause position between different storms. This has the effect of blurring out the plasmopause position, and hence, the “knee” is not seen in Figure 8. However, we still expect the plasmopause to retreat in this region due to enhanced magnetospheric convection. In Figures 8c and 8d, for the innermost station pair, the plasma mass density decreases as expected from plasmopause erosion. The O'Brien and Moldwin (2003) plasmopause model shows that the plasmopause distance at noon will decrease to $L < 3$ for a -100 nT storm, which supports our observation of decreasing plasma mass density for $L \sim 4$.

There may still be an increase in the average ion mass due to higher densities of O^+ or an increase in the mass density of the energetic population, as suggested in Section 5.1. However, the observations suggest that any increase in the average ion mass is inferior to the cold plasma loss of mass from plasmopause erosion observed for $L < 4$. Hence, we see the opposite behavior in the eigenfrequencies for the innermost L-shells.

6. Conclusions

This study determined how the eigenfrequency continuum changed during geomagnetic storms and how this was controlled by the underlying magnetic field strength and plasma mass density. We analyzed the eigenfrequencies of magnetic field lines during 132 storms using a superposed multiple-epoch analysis on cross-phase spectra derived from ground-based magnetometer stations in the range $3.15 \leq L \leq 6.42$. This region corresponds to a key region during geomagnetic storms because of its proximity to the ring current and radiation belts. This has enabled us to determine the average time evolution of the fundamental eigenfrequency during each of the three phases of a geomagnetic storm. We then solved the Alfvén wave equation of Singer et al. (1981) using the TS05 magnetic field model of Tsyganenko and Sitnov (2005) to determine how the plasma mass density changes directly for the first time.

It was found that the fundamental eigenfrequency decreased in all dayside MLT sectors during the main phase for $L > 4$ and this corresponded to a weaker magnetic field and an increased plasma mass density, with a clear MLT dependence on the reduction. The changes in both of these dependencies would decrease the eigenfrequency. We suggest that the increase in plasma mass density is caused by an increase in Oxygen ion density.

For $L < 4$, the eigenfrequency increased relative to the quiet time value. This was accompanied by a decrease in the plasma mass density, which is thought to be caused by plasmopause erosion during the main phase of a storm. However, the magnetic field strength still decreased, suggesting that the plasma mass density has a stronger influence over the eigenfrequency than the magnetic field at these locations.

Data Availability Statement

The data are available at the website (<http://space.fmi.fi/image/beta/>). The OMNI solar wind and geomagnetic indices data are publicly available from the NASA Space Physics Data Facility, Goddard Space Flight Center (<http://omniweb.gsfc.nasa.gov/ow.html>). This research used the SPECTRE High Performance Com-

puting Facility at the University of Leicester. The list of geomagnetic storm events used in this study is available in the supporting information.

Acknowledgments

S. J. W. was supported by NERC Studentship NE/L002493/1. I. J. R. was supported by STFC Grants ST/S000240/1 and ST/N000722/1 and NERC Grants NE/P017150/1 and NE/P017185/1. J. K. S. was supported by NERC Grant NE/P017185/1. M.-T. W was supported by NERC Grant NE/P001556/1. T. K. Y. was supported by STFC Grant ST/S000429/1. The authors would like to thank the IMAGE magnetometer team for providing the data.

References

Akasofu, S.-I., Chapman, S., & Venkatesan, D. (1963). The main phase of great magnetic storms. *Journal of Geophysical Research* (1896-1977), 68(11), 3345–3350. <https://doi.org/10.1029/JZ068i011p03345>

Angerami, J. J., & Thomas, J. O. (1964). Studies of planetary atmospheric: 1. The distribution of electrons and ions in the Earth's exosphere. *Journal of Geophysical Research*, 69(21), 4537–4560. <https://doi.org/10.1029/JZ069i021p04537>

Berube, D., Moldwin, M. B., & Ahn, M. (2006). Computing magnetospheric mass density from field line resonances in a realistic magnetic field geometry. *Journal of Geophysical Research*, 111, A08206. <https://doi.org/10.1029/2005JA011450>

Berube, D., Moldwin, M. B., & Weygand, J. M. (2003). An automated method for the detection of field line resonance frequencies using ground magnetometer techniques. *Journal of Geophysical Research*, 108(A9), 1348. <https://doi.org/10.1029/2002JA009737>

Bland, E. C., McDonald, A. J., Menk, F. W., & Devlin, J. C. (2014). Multipoint visualization of ULF oscillations using the Super Dual Auroral Radar Network. *Geophysical Research Letters*, 41, 6314–6320. <https://doi.org/10.1002/2014GL061371>

Carpenter, D. L., & Smith, R. L. (1964). Whistler measurements of electron density in the magnetosphere. *Reviews of Geophysics*, 2(3), 415–441. <https://doi.org/10.1029/RG002i003p00415>

Chapman, S., & Ferraro, V. C. A. (1930). A new theory of magnetic storms. *Nature*, 126, 129–130. <https://doi.org/10.1038/126129a0DO>

Chappell, C. R., Harris, K. K., & Sharp, G. W. (1971). The dayside of the plasmasphere. *Journal of Geophysical Research*, 76(31), 7632–7647. <https://doi.org/10.1029/JA076i031p07632>

Chi, P. J., Engebretson, M. J., Moldwin, M. B., Russell, C. T., Mann, I. R., Hairston, M. R., et al. (2013). Sounding of the plasmasphere by Mid-continent MAGnetoseismic Chain (McMAC) magnetometers. *Journal of Geophysical Research: Space Physics*, 118, 3077–3086. <https://doi.org/10.1002/jgra.50274>

Chi, P. J., Russell, C. T., Foster, J. C., Moldwin, M. B., Engebretson, M. J., & Mann, I. R. (2005). Density enhancement in plasmasphere-ionosphere plasma during the 2003 Halloween Superstorm: Observations along the 330th magnetic meridian in North America. *Geophysical Research Letters*, 32(3). <https://doi.org/10.1029/2004GL021722>

Chisham, G., Lester, M., Milan, S. E., Freeman, M. P., Bristow, W. A., Grocott, A., et al. (2007). A decade of the Super Dual Auroral Radar Network (SuperDARN): Scientific achievements, new techniques and future directions. *Surveys Geophysics*, 28(1), 33–109. <https://doi.org/10.1007/s10712-007-9017-8>

Corpo, A. D., Vellante, M., Heilig, B., Pietropaolo, E., Reda, J., & Lichtenberger, J. (2018). Observing the cold plasma in the Earth's magnetosphere with the EMMA network. *Annals of Geophysics*, 61(0), 33. <https://doi.org/10.4401/ag-7751>

Cummings, W. D., O'Sullivan, R. J., & Coleman, P. J. (1969). Standing Alfvén waves in the magnetosphere. *Journal of Geophysical Research*, 74(3), 778–793. <https://doi.org/10.1029/JA074i003p00778>

Dent, Z. C., Mann, I. R., Goldstein, J., Menk, F. W., & Ozeke, L. G. (2006). Plasmaspheric depletion, refilling, and plasmopause dynamics: A coordinated ground-based and IMAGE satellite study. *Journal of Geophysical Research*, 111, A03205. <https://doi.org/10.1029/2005JA011046>

Denton, R. E., Takahashi, K., Galkin, I. A., Nsumei, P. A., Huang, X., Reinisch, B. W., et al. (2006). Distribution of density along magnetospheric field lines. *Journal of Geophysical Research*, 111, A04213. <https://doi.org/10.1029/2005JA011414>

Du, A., Sun, W., Xu, W., & Gao, X. (2005). The frequency variation of Pc5 ULF waves during a magnetic storm. *Earth, Planets and Space*, 57(7), 619–625. <https://doi.org/10.1186/BF03351841>

Engebretson, M. J., & Cahill Jr., L. J. (1981). Pc5 pulsations observed during the June 1972 geomagnetic storm. *Journal of Geophysical Research*, 86(A7), 5619–5631. <https://doi.org/10.1029/JA086iA07p05619>

Gkioulidou, M., Ohtani, S., Ukhorskiy, A. Y., Mitchell, D. G., Takahashi, K., Spence, H. E., et al. (2019). Low-energy (<keV) O⁺ ion outflow directly into the inner magnetosphere: Van Allen Probes observations. *Journal of Geophysical Research: Space Physics*, 124, 405–419. <https://doi.org/10.1029/2018JA025862>

Gonzalez, W. D., Joselyn, J. A., Kamide, Y., Kroehl, H. W., Rostoker, G., Tsurutani, B. T., & Vasyliunas, V. M. (1994). What is a geomagnetic storm? *Journal of Geophysical Research*, 99(A4), 5771–5792. <https://doi.org/10.1029/93JA02867>

Greenwald, R. A., Baker, K. B., Dudeney, J. R., Pinnock, M., Jones, T. B., Thomas, E. C., et al. (1995). DARN/SuperDARN. *Space Science Reviews*, 71(1), 761–796. <https://doi.org/10.1007/BF00751350>

Huang, C.-L., Spence, H. E., Singer, H. J., & Tsyganenko, N. A. (2008). A quantitative assessment of empirical magnetic field models at geosynchronous orbit during magnetic storms. *Journal of Geophysical Research*, 113(A4), A04208. <https://doi.org/10.1029/2007JA012623>

Hughes, W. J., & Southwood, D. J. (1976). The screening of micropulsation signals by the atmosphere and ionosphere. *Journal of Geophysical Research*, 81(19), 3234–3240. <https://doi.org/10.1029/JA081i019p03234>

Hutchinson, J. A., Wright, D. M., & Milan, S. E. (2011). Geomagnetic storms over the last solar cycle: A superposed epoch analysis. *Journal of Geophysical Research*, 116, A09211. <https://doi.org/10.1029/2011JA016463>

Iyemori, T. (1990). Storm-time magnetospheric currents inferred from mid-latitude geomagnetic field variations. *Journal of Geomagnetism and Geolectricity*, 42(11), 1249–1265. <https://doi.org/10.5636/jgg.42.1249>

Kale, Z. C., Mann, I. R., Waters, C. L., Goldstein, J., Menk, F. W., & Ozeke, L. G. (2007). Ground magnetometer observation of a cross-phase reversal at a steep plasmopause. *Journal of Geophysical Research*, 112, A10222. <https://doi.org/10.1029/2007JA012367>

Kale, Z. C., Mann, I. R., Waters, C. L., Vellante, M., Zhang, T. L., & Honary, F. (2009). Plasmaspheric dynamics resulting from the Halloween 2003 geomagnetic storms. *Journal of Geophysical Research*, 114, A08204. <https://doi.org/10.1029/2009JA014194>

Kistler, L. M., Mouikis, C. G., Spence, H. E., Menz, A. M., Skoug, R. M., Funsten, H. O., et al. (2016). The source of O⁺ in the storm time ring current. *Journal of Geophysical Research: Space Physics*, 121, 5333–5349. <https://doi.org/10.1002/2015JA022204>

Kronberg, E. A., Ashour-Abdalla, M., Dandouras, I., Delcourt, D. C., Grigorenko, E. E., Kistler, L. M., et al. (2014). Circulation of heavy ions and their dynamical effects in the magnetosphere: Recent observations and models. *Space Science Reviews*, 184(1), 173–235. <https://doi.org/10.1007/s11214-014-0104-0>

Lee, E. A., Mann, I. R., Loto'aniu, T. M., & Dent, Z. C. (2007). Global Pc5 pulsations observed at unusually low L during the great magnetic storm of 24 March 1991. *Journal of Geophysical Research*, 112, A05208. <https://doi.org/10.1029/2006JA011872>

Luhr, H. (1994). The IMAGE magnetometer network. *STEP International Newsletter*, 4, 4–6.

Mardia, K. V., & Jupp, P. E. (2000). *Directional statistics*. Chichester, UK: John Wiley and Sons, Ltd. <https://doi.org/10.1002/9780470316979>

- Menk, F., Kale, Z., Sciffer, M., Robinson, P., Waters, C., Grew, R., et al. (2014). Remote sensing the plasmasphere, plasmopause, plumes and other features using ground-based magnetometers. *Journal of Space Weather and Space Climate*, 4, A34. <https://doi.org/10.1051/swsc/2014030>
- Menk, F. W., Mann, I. R., Smith, A. J., Waters, C. L., Clilverd, M. A., & Milling, D. K. (2004). Monitoring the plasmopause using geomagnetic field line resonances. *Journal of Geophysical Research*, 109, A04216. <https://doi.org/10.1029/2003JA010097>
- Menk, F. W., Orr, D., Clilverd, M. A., Smith, A. J., Waters, C. L., Milling, D. K., & Fraser, B. J. (1999). Monitoring spatial and temporal variations in the dayside plasmasphere using geomagnetic field line resonances. *Journal of Geophysical Research*, 104(A9), 19,955–19,969. <https://doi.org/10.1029/1999JA900205>
- Menk, F. W., & Waters, C. L. (2013). *Magnetoseismology ground-based remote sensing of the Earth's magnetosphere*. Weinheim: John Wiley & Sons, Inc. <https://doi.org/10.1002/9783527652051>
- Min, K., Bortnik, J., Denton, R. E., Takahashi, K., Lee, J., & Singer, H. J. (2013). Quiet time equatorial mass density distribution derived from AMPTE/CCE and GOES using the magnetoseismology technique. *Journal of Geophysical Research: Space Physics*, 118, 6090–6105. <https://doi.org/10.1002/jgra.50563>
- Mitani, K., Seki, K., Keika, K., Gkioulidou, M., Lanzerotti, L. J., Mitchell, D. G., et al. (2019). Statistical study of selective oxygen increase in high-energy ring current ions during magnetic storms. *Journal of Geophysical Research: Space Physics*, 124, 3193–3209. <https://doi.org/10.1029/2018JA026168>
- Murphy, K. R., Mann, I. R., Rae, I. J., Sibeck, D. G., & Watt, C. E. J. (2016). Accurately characterizing the importance of wave-particle interactions in radiation belt dynamics: The pitfalls of statistical wave representations. *Journal of Geophysical Research: Space Physics*, 121, 7895–7899. <https://doi.org/10.1002/2016JA022618>
- Murphy, K. R., Watt, C. E. J., Mann, I. R., Jonathan Rae, I., Sibeck, D. G., Boyd, A. J., et al. (2018). The global statistical response of the outer radiation belt during geomagnetic storms. *Geophysical Research Letters*, 45, 3783–3792. <https://doi.org/10.1002/2017GL076674>
- Nosé, M., Takahashi, K., Anderson, R. R., & Singer, H. J. (2011). Oxygen torus in the deep inner magnetosphere and its contribution to recurrent process of O⁺-rich ring current formation. *Journal of Geophysical Research*, 116, A10224. <https://doi.org/10.1029/2011JA016651>
- O'Brien, T. P., & Moldwin, M. B. (2003). Empirical plasmopause models from magnetic indices. *Geophysical Research Letters*, 30(4), 1152. <https://doi.org/10.1029/2002GL016007>
- Orr, D., & Matthew, J. A. (1971). The variation of geomagnetic micropulsation periods with latitude and the plasmopause. *Planetary and Space Science*, 19(8), 897–905. [https://doi.org/10.1016/0032-0633\(71\)90141-3](https://doi.org/10.1016/0032-0633(71)90141-3)
- Poulter, E. M., Allan, W., Keys, J. G., & Nielsen, E. (1984). Plasmatrough ion mass densities determined from ULF pulsation eigenperiods. *Planetary and Space Science*, 32(9), 1069–1078. [https://doi.org/10.1016/0032-0633\(84\)90132-6](https://doi.org/10.1016/0032-0633(84)90132-6)
- Rae, I., Jonathan, Mann, I. R., Murphy, K. R., Ozeke, L. G., Milling, D. K., Chan, A. A., et al. (2012). Ground-based magnetometer determination of in situ Pc4-5 ULF electric field wave spectra as a function of solar wind speed. *Journal of Geophysical Research*, 117, A04221. <https://doi.org/10.1029/2011JA017335>
- Rae, I. J., Murphy, K. R., Watt, C. E. J., Sandhu, J. K., Georgiou, M., Degeling, A. W., et al. (2019). How do ultra-low frequency waves access the inner magnetosphere during geomagnetic storms? *Geophysical Research Letters*, 46, 10,699–10,709. <https://doi.org/10.1029/2019GL082395>
- Rankin, R., Kabin, K., & Marchand, R. (2006). Alfvénic field line resonances in arbitrary magnetic field topology. *Advances in Space Research*, 38(8), 1720–1729. <http://www.sciencedirect.com/science/article/pii/S0273117705011452>
- Salat, A., & Tataronis, J. A. (2000). Conditions for existence of orthogonal coordinate systems oriented by magnetic field lines. *Journal of Geophysical Research*, 105(A6), 13,055–13,062. <https://doi.org/10.1029/1999JA000221>
- Sandhu, J. K., Yeoman, T. K., Fear, R. C., & Dandouras, I. (2016). A statistical study of magnetospheric ion composition along the geomagnetic field using the Cluster spacecraft for L values between 5.9 and 9.5. *Journal of Geophysical Research: Space Physics*, 121, 2194–2208. <https://doi.org/10.1002/2015JA022261>
- Sandhu, J. K., Yeoman, T. K., James, M. K., Rae, I. J., & Fear, R. C. (2018). Variations of high-latitude geomagnetic pulsation frequencies: A comparison of time-of-flight estimates and IMAGE magnetometer observations. *Journal of Geophysical Research: Space Physics*, 123, 567–586. <https://doi.org/10.1002/2017JA024434>
- Sandhu, J. K., Yeoman, T. K., & Rae, I. J. (2018). Variations of field line eigenfrequencies with ring current intensity. *Journal of Geophysical Research: Space Physics*, 123, 9325–9339. <https://doi.org/10.1029/2018JA025751>
- Sandhu, J. K., Yeoman, T. K., Rae, I. J., Fear, R. C., & Dandouras, I. (2017). The dependence of magnetospheric plasma mass loading on geomagnetic activity using Cluster. *Journal of Geophysical Research: Space Physics*, 122, 9371–9395. <https://doi.org/10.1002/2017JA024171>
- Singer, H. J., Southwood, D. J., Walker, R. J., & Kivelson, M. G. (1981). Alfvén wave resonances in a realistic magnetospheric magnetic field geometry. *Journal of Geophysical Research*, 86(A6), 4589–4596. <https://doi.org/10.1029/JA086iA06p04589>
- Southwood, D. J. (1974). Some features of field line resonances in the magnetosphere. *Planetary and Space Science*, 22(3), 483–491. [https://doi.org/10.1016/0032-0633\(74\)90078-6](https://doi.org/10.1016/0032-0633(74)90078-6)
- Stewart, B. (1861). On the great magnetic disturbance which extended from August 28 to September 7, 1859, as recorded by photography at the Kew Observatory. *Philosophical Transactions of the Royal Society of London*, 151, 423–430. <https://doi.org/10.1098/rstl.1861.0023>
- Takahashi, K., & Denton, R. E. (2007). Magnetospheric seismology using multiharmonic toroidal waves observed at geosynchronous orbit. *Journal of Geophysical Research*, 112, A05204. <https://doi.org/10.1029/2006JA011709>
- Takahashi, K., Denton, R. E., Anderson, R. R., & Hughes, W. J. (2006). Mass density inferred from toroidal wave frequencies and its comparison to electron density. *Journal of Geophysical Research*, 111, A01201. <https://doi.org/10.1029/2005JA011286>
- Takahashi, K., Denton, R. E., & Gallagher, D. (2002). Toroidal wave frequency at L = 6–10: Active Magnetospheric Particle Tracer Explorers/CCE observations and comparison with theoretical model. *Journal of Geophysical Research*, 107(A2), SMP 2–1–SMP 2–14. <https://doi.org/10.1029/2001JA000197>
- Takahashi, K., Denton, R. E., & Singer, H. J. (2010). Solar cycle variation of geosynchronous plasma mass density derived from the frequency of standing Alfvén waves. *Journal of Geophysical Research*, 115, A07207. <https://doi.org/10.1029/2009JA015243>
- Takahashi, K., Lee, D., Merkin, V. G., Lyon, J. G., & Hartinger, M. D. (2016). On the origin of the dawn-dusk asymmetry of toroidal Pc5 waves. *Journal of Geophysical Research: Space Physics*, 121, 9632–9650. <https://doi.org/10.1002/2016JA023009>
- Takahashi, K., & McPherron, R. L. (1984). Standing hydromagnetic oscillations in the magnetosphere. *Planetary and Space Science*, 32(11), 1343–1359. [https://doi.org/10.1016/0032-0633\(84\)90078-3](https://doi.org/10.1016/0032-0633(84)90078-3)
- Takasaki, S., Kawano, H., Tanaka, Y., Yoshikawa, A., Seto, M., Iizima, M., et al. (2006). A significant mass density increase during a large magnetic storm in October 2003 obtained by ground-based ULF observations at L ~ 1.4. *Earth Planets Space*, 58, 617–622. <https://doi.org/10.1186/BF03351959>

- Tsyganenko, N. A. (1996). Effects of the solar wind conditions on the global magnetospheric configuration as deduced from data-based field models. In *Proc. third International Conference on Substorms* (pp. 181–185). ESA.
- Tsyganenko, N. A., & Sitnov, M. I. (2005). Modeling the dynamics of the inner magnetosphere during strong geomagnetic storms. *Journal of Geophysical Research*, *110*, A03208. <https://doi.org/10.1029/2004JA010798>
- Walach, M.-T., & Grocott, A. (2019). SuperDARN observations during geomagnetic storms, geomagnetically active times, and enhanced solar wind driving. *Journal of Geophysical Research: Space Physics*, *124*, 5828–5847. <https://doi.org/10.1029/2019JA026816>
- Wanliss, J. A., & Showalter, K. M. (2006). High-resolution global storm index: Dst versus SYM-H. *Journal of Geophysical Research*, *111*, A02202. <https://doi.org/10.1029/2005JA011034>
- Warner, M. R., & Orr, D. (1979). Time of flight calculations for high latitude geomagnetic pulsations. *Planetary and Space Science*, *27*(5), 679–689. [https://doi.org/10.1016/0032-0633\(79\)90165-X](https://doi.org/10.1016/0032-0633(79)90165-X)
- Waters, C. L., Menk, F. W., & Fraser, B. J. (1991). The resonance structure of low latitude Pc3 geomagnetic pulsations. *Geophysical Research Letters*, *18*(12), 2293–2296. <https://doi.org/10.1029/91GL02550>
- Waters, C. L., Samson, J. C., & Donovan, E. F. (1996). Variation of plasmatrough density derived from magnetospheric field line resonances. *Journal of Geophysical Research*, *101*(A11), 24,737–24,745. <https://doi.org/10.1029/96JA01083>
- Wharton, S. J., Wright, D. M., Yeoman, T. K., James, M. K., & Sandhu, J. K. (2018). Cross-phase determination of ultralow frequency wave harmonic frequencies and their associated plasma mass density distributions. *Journal of Geophysical Research: Space Physics*, *123*, 6231–6250. <https://doi.org/10.1029/2018JA025487>
- Wharton, S. J., Wright, D. M., Yeoman, T. K., James, M. K., & Sandhu, J. K. (2019). The variation of resonating magnetospheric field lines with changing geomagnetic and solar wind conditions. *Journal of Geophysical Research: Space Physics*, *124*, 5353–5375. <https://doi.org/10.1029/2019JA026848>
- Wharton, S. J., Wright, D. M., Yeoman, T. K., & Reimer, A. S. (2019). Identifying ULF wave eigenfrequencies in SuperDARN backscatter using a Lomb-Scargle cross-phase analysis. *Journal of Geophysical Research: Space Physics*, *124*, 996–1012. <https://doi.org/10.1029/2018JA025859>
- Wild, J. A., Yeoman, T. K., & Waters, C. L. (2005). Revised time-of-flight calculations for high-latitude geomagnetic pulsations using a realistic magnetospheric magnetic field model. *Journal of Geophysical Research*, *110*, A11206. <https://doi.org/10.1029/2004JA010964>
- Yue, C., Bortnik, J., Li, W., Ma, Q., Wang, C.-P., Thorne, R. M., et al. (2019). Oxygen ion dynamics in the Earth's ring current: Van Allen Probes observations. *Journal of Geophysical Research: Space Physics*, *124*, 7786–7798. <https://doi.org/10.1029/2019JA026801>